The Astrophysical Journal, 784:164 (15pp), 2014 April 1 doi:10.1088/0004-637X/784/2/164
© 2014. The American Astronomical Society. All rights reserved. Printed in the U.S.A.

GLOBAL-SCALE CONSEQUENCES OF MAGNETIC-HELICITY INJECTION AND CONDENSATION ON THE SUN

Duncan H. Mackay[1], C. Richard DeVore[2,3], and Spiro K. Antiochos[3]
[1] School of Mathematics and Statistics, University of St Andrews, North Haugh, St Andrews, Fife, KY16 9SS, UK; dhm@st-and.ac.uk
[2] Naval Research Laboratory, Washington, DC 20375, USA
[3] NASA Goddard Space Flight Center, Greenbelt, MD 20771, USA
Received 2013 July 10; accepted 2014 February 7; published 2014 March 18

ABSTRACT

In the recent paper of Antiochos, a new concept for the injection of magnetic helicity into the solar corona by small-scale convective motions and its condensation onto polarity inversion lines (PILs) was developed. We investigate this concept through global simulations of the Sun's photospheric and coronal magnetic fields, and compare the results with the hemispheric pattern of solar filaments. Assuming that the vorticity of the cells is predominantly counterclockwise/clockwise in the northern/southern hemisphere, the convective motions inject negative/positive helicity into each hemisphere. The simulations show that: (1) on a north–south oriented PIL, both differential rotation and convective motions inject the same sign of helicity, which matches that required to reproduce the hemispheric pattern of filaments. (2) On a high-latitude east–west oriented polar crown or subpolar crown PIL, the vorticity of the cells has to be approximately 2–3 times greater than the local differential-rotation gradient in order to overcome the incorrect sign of helicity injection from differential rotation. (3) In the declining phase of the cycle, as a bipole interacts with the polar field, in some cases, helicity condensation can reverse the effect of differential rotation along the east–west lead arm but not in all cases. The results show that this newly developed concept of magnetic helicity injection and condensation, in conjunction with the mechanisms used in Yeates et al., is a viable explanation for the hemispheric pattern of filaments. Future observational studies should focus on examining the vorticity component within convective motions to determine both its magnitude and latitudinal variation relative to the differential-rotation gradient on the Sun.

Key words: magnetic fields – Sun: activity – Sun: corona

Online-only material: color figures

1. INTRODUCTION

Solar filaments (a.k.a. prominences) exist across a wide range of latitudes on the Sun. They form everywhere from the active latitudes all the way to the polar crown. As magnetic flux is pushed from low to high latitudes during the 11 yr activity cycle, solar filaments are seen to "rush" to the poles (Mouradian & Soru-Escaut 1994; Minarovjech et al. 1998). A signature of the reversal of the Sun's polar field in each hemisphere is the disappearance of the high-latitude polar crown filaments. While solar filaments may form over a wide range of latitudes, they always form above polarity inversion lines (PILs) in the photospheric magnetic field. However, the existence of a PIL is not a sufficient condition for the existence of a filament. There must also be a filament channel at the height of the chromosphere (Martres et al. 1966; Gaizauskas 1998). In its simplest terms, a filament channel is a region of the chromosphere surrounding a PIL where there exists a dominant horizontal field which lies nearly parallel to the PIL. A more formal definition of a filament channel can be found in the papers of Foukal (1971a, 1971b) and Martin (1998). Direct observations of the orientation of magnetic fields within solar prominences (Rust 1967; Leroy et al. 1983, 1984) show that the field is oriented mainly along the long axis of the filament, nearly parallel to the PIL, as is the case in the surrounding filament channel.

A wide variety of models has been developed over the years to explain the origin of the axial magnetic field in filaments and filament channels (for a detailed discussion, see Section 5.3 of Mackay et al. 2010). In the majority of models, the presence of the horizontal magnetic field nearly parallel to the PIL indicates that the field is highly nonpotential. Therefore, filaments and filament channels are indicators of the location and concentration of free magnetic energy in the solar corona, which in turn is key to explaining many eruptive phenomena. One surprising feature of the magnetic field in solar prominences/filaments is that the orientation of the dominant axial field exhibits a large-scale hemispheric chirality pattern (Martin et al. 1994). Filaments and filament channels of so-called dextral chirality dominate in the northern hemisphere, while those of sinistral chirality dominate in the southern hemisphere. A dextral filament (or filament channel) is one in which the dominant axial magnetic field points to the right, as seen from an observer standing on the positive-polarity side of the PIL and looking toward the PIL. Correspondingly, from the same reference point, a sinistral filament has an axial magnetic field that points to the left. In force-free magnetic-field models of filaments (Aulanier & Démoulin 1998; Mackay et al. 1999; van Ballegooijen 2004), this chirality is directly related to the dominant sign of magnetic helicity that is contained within the filament and its channel. Dextral filaments contain predominantly negative helicity; sinistral filaments have mainly positive helicity. Due to challenges in determining the orientation of the axial magnetic field in filaments (Gaizauskas 2002), often the hemispheric pattern of filaments is determined indirectly through the orientation of the filament barbs (Pevtsov et al. 2003; Yeates et al. 2007). One noteworthy feature of the hemispheric pattern of filaments and channels is that, in each hemisphere, exceptions to the rule do exist. Therefore, any model that aims to account for the hemispheric pattern must not only produce the dominant pattern but also allow exceptions to occur.

Previous studies have considered the origin of the hemispheric pattern by modeling the evolution of either idealized magnetic

distributions (Mackay & van Ballegooijen 2001, 2005) or observed distributions that can be compared directly with subsequent measurements (van Ballegooijen et al. 1998; Mackay et al. 2000). The most detailed study to date was carried out by Yeates et al. (2007, 2008), who compared the observed chirality of 109 filaments observed over a six-month interval with nonpotential magnetic fields deduced from the global evolution model of van Ballegooijen et al. (2000) and Mackay & van Ballegooijen (2006). It was found that, if the transport effects of differential rotation, meridional flow, and surface diffusion are combined with newly emerging bipoles in the northern/southern hemisphere already containing negative/positive helicity, then a 96% agreement can be obtained between the observed chirality of the filaments and that produced by the model. The agreement was equally good for both the dominant and minority chirality in each hemisphere. This agreement was, however, mainly for filaments lying below 60° latitude. In a further study, Yeates & Mackay (2012) simulated the global corona for the entire length of cycle 23. By considering the latitudinal distribution of chirality in both hemispheres, they showed that dextral/sinistral skew can dominate at high latitudes in the northern/southern hemispheres during the rising phase and rush to the poles. However, they also found that, in the declining phase, sinistral skew was dominant at high latitudes in the northern hemisphere and dextral in the southern hemisphere. Thus far, no detailed observational studies of filament chirality have been carried out in the declining phase of the solar cycle to test these predictions.

Yeates & Mackay (2009a) discussed the mechanisms that produced the chirality patterns in the simulations of Yeates et al. (2008) and Yeates & Mackay (2012). First and foremost is the injection of helicity by the applied large-scale boundary motions, in particular solar differential rotation, which injects both positive and negative helicity into each hemisphere depending upon the orientation of the PIL at the surface (e.g., DeVore 2000, and references therein). At north–south PILs, such as those that typically occur within active regions, the helicity injected is negative in the northern hemisphere and positive in the southern, in accord with the dominant pattern of filament chirality. At east–west PILs, on the other hand, such as those that sometimes arise between active regions and routinely occur at the polar crown between the active-latitude and polar fluxes, the helicity injected is positive in the north and negative in the south, in opposition to the dominant chirality pattern. Consequently, the applied boundary motions alone were found to be insufficient to explain the observations. To recover the hemispheric pattern, the injection of magnetic helicity associated with newly emerging bipolar flux was also required. The bipoles contained an internal helicity that matched the observations of Pevtsov et al. (1995), negative in the northern hemisphere and positive in the southern, but also contained a mutual helicity of either sign due to the interaction of the new bipole with the surrounding background field. This injection of helicity occurred in a sporadic manner in localized regions and then was transported across the solar surface along with the PILs. However, once lost due to the ejections of flux ropes (Yeates & Mackay 2009b), which occur when a critical amount of shear accumulates along a section of the PIL, helicity of the correct sign cannot always be regenerated in situ. The chirality of the east–west filament channels, in particular those at the polar crown, then progressively departed ever farther from the dominant hemispheric pattern, as Yeates & Mackay (2012) found in the declining phase of the cycle.

Recently, Antiochos (2013) proposed a new helicity-condensation model for the formation of filament channels that, in principle, could resolve the possible outstanding incompatibilities between flux-transport simulations and the observed hemispheric patterns of chirality. In his model, filament channels form through a three-stage process of helicity injection, transfer, and condensation that acts on the chromospheric and coronal magnetic fields, as follows. (1) Helicity is injected into the overlying atmosphere by small-scale, vortical motions occurring at the photosphere. These motions are associated with both the granular and supergranular convection, in general, although the latter dominates due to the much larger spatial scale and lifetime of its cells. If the motions are predominantly counterclockwise in the northern hemisphere and clockwise in the southern, in concurrence with the observed sense of the Sun's differential rotation, then the resultant magnetic twist is left-handed (or dextral) in the north and right-handed (or sinistral) in the south. This pattern is fully consistent with the dominant hemispheric pattern of chirality. (2) Within a magnetically unipolar region, neighboring flux concentrations having the same sense of twist have oppositely directed horizontal field components where they come into contact. Therefore, those fields are favorably disposed to reconnect, which transfers the twist field encircling two individual flux elements to the outer perimeter of their combined flux concentrations. This process occurs across the entire spectrum of flux-concentration sizes, redistributing the twist injected at the small scales of the vortical motion to the largest scale available—the extent of the unipolar region. (3) At the boundaries between regions of opposite magnetic polarity that have the same sense of twist, the horizontal field is in the same direction on either side of the PIL. Thus, reconnection cannot occur there, and the twist field component accumulates at the PIL. The result is an increasingly strong axial field and magnetic helicity that "condense" along the PIL, giving the model its name, and which are precisely the key characteristics of observed filament channels on the Sun.

The sign and strength of the axial field and helicity at the PIL in the helicity-condensation model depend sensitively upon the associated sign and strength of the underlying vortical motions. In addition, the consequences of those motions may be enhanced or reduced by cooperation or competition, respectively, with the other flux-transport processes known to influence the formation of filament channels. The objective of this paper is to take a first step toward quantifying the impact of helicity condensation on the formation of solar filament channels, within the context of global-scale modeling of the coronal magnetic field. Confirmation of the three-stage process of helicity injection, transfer, and condensation through high-resolution modeling of the vortical flows, the reconnection between flux elements, and the accumulation of twist at the perimeter of the region of vortical flow is reported by Zhao et al. (2013). In this investigation, of necessity, we employ a large-scale, averaged representation of those small-scale dynamics, as described below.

The paper is structured as follows. In Section 2, the global evolutionary model for the corona is described (Section 2.1), along with the model for the large-scale consequences of small-scale helicity injection by vortical cellular motions (Section 2.2; see also the Appendix). In Section 3, some simple test simulations are carried out to quantify the effect of the helicity injection and to compare it to standard surface flux-transport calculations. Next, in Sections 4 and 5, results are shown for a variety of magnetic field configurations consistent with those found on the Sun in both the rising and declining phases of the solar cycle, in which the helicity injection acts in concert with the usual flux-transport processes. Finally, in Section 6,

a summary of our results and discussions of their consequences and of possible future studies on this topic are given.

2. MODELS

To simulate the evolution of the Sun's large-scale magnetic field (Mackay & Yeates 2012), a combination of magnetic-flux transport (Sheeley 2005) and magneto-frictional relaxation (van Ballegooijen et al. 2000; Mackay & van Ballegooijen 2006) simulations is applied. In addition, a new model for the injection of magnetic helicity into the large-scale corona, due to small-scale convective cells, is included. In the combined models, the Sun's large-scale magnetic field, $\mathbf{B}(= B_r, B_\theta, B_\phi) = \nabla \times \mathbf{A}$, is evolved by the induction equation, where r is the radial distance from the Sun's center, θ is the co-latitude, and ϕ is the azimuthal angle.

2.1. Global Evolution

To describe the evolution of magnetic fields in the photosphere, the induction equation at $r = R_\odot$ is prescribed to impose the large-scale flows of differential rotation (Snodgrass 1983) and meridional circulation (Duvall 1979). In addition, the magnetic field is subject to diffusion by small-scale flows such as supergranulation (Leighton 1964), described as surface diffusion. This surface diffusion leads to the cancellation of opposite polarity magnetic fields when they encounter one another at PILs. These effects are applied as boundary conditions to the time derivatives of the horizontal components of the vector potential A_θ and A_ϕ (therefore on B_r),

$$\frac{\partial A_\theta}{\partial t} = +u_\phi B_r - \frac{D}{r \sin\theta}\frac{\partial B_r}{\partial \phi}, \quad (1)$$

$$\frac{\partial A_\phi}{\partial t} = -u_\theta B_r + \frac{D}{r}\frac{\partial B_r}{\partial \theta}, \quad (2)$$

where u_ϕ is the azimuthal velocity, u_θ is the meridional flow velocity, and D is the photospheric diffusion constant ($D = 450\,\mathrm{km^2\,s^{-1}}$; see DeVore et al. 1985), all of which are determined from observations. The azimuthal velocity is taken to be of the form

$$u_\phi = \Omega(\theta) r \sin\theta,$$

where $\Omega(\theta)$ is the angular velocity of differential rotation relative to the Carrington frame which rotates at 13.20 deg day^{-1} (Snodgrass 1983),

$$\Omega(\theta) = 0.18 - 2.30\cos^2\theta - 1.62\cos^4\theta \,\mathrm{deg\,day^{-1}}.$$

The poleward meridional flow is chosen such that $u_\theta = 0$ at the latitudinal boundaries ($\theta_{\min}$, $\theta_{\max}$),

$$u_\theta = C\cos\left[\frac{\pi(\theta_{\max} + \theta_{\min} - 2\theta)}{2(\theta_{\max} - \theta_{\min})}\right]\cos\theta,$$

and C is chosen such that the peak velocity at mid-latitudes is 15 m s^{-1}.

Within the coronal volume, the magnetic field evolves in response to these motions through the ideal induction equation,

$$\frac{\partial \mathbf{A}}{\partial t} = \mathbf{v} \times \mathbf{B} + \mathbf{H}_{sg}, \quad (3)$$

where $\mathbf{v}(\mathbf{r}, t)$ is the plasma velocity and $\mathbf{H}_{sg}$ represents the supergranular helicity injection term to be described in detail in Section 2.2. Since all of the photospheric boundary motions described above are very slow compared to the coronal Alfvén speed, and the plasma beta is low there, we expect the coronal magnetic field evolution to closely approximate a sequence of quasi-steady force-free states. Furthermore, we are interested primarily in the long-lived structure of the field, not in the high-frequency dynamics including all MHD waves; therefore, we can use the magneto-frictional method as in Yang et al. (1986) to capture the essential evolution. We assume that the coronal plasma velocity is given by

$$\mathbf{v} = \frac{1}{\nu}\frac{\mathbf{j} \times \mathbf{B}}{B^2} + v_o e^{-(2.5\,R_\odot - r)/r_w}\hat{\mathbf{r}}.$$

where $\mathbf{j} = \nabla \times \mathbf{B}$. The first term on the right hand side reflects the fact that in the corona, the Lorentz force is dominant (low beta condition). The effect of this "frictional" term is that, when any field departs from a force-free state—as a result of boundary driving, for example—the magnetic forces in the corona act to return the field to a force-free state (generally, a nonlinear force-free field). The second term represents a radial outflow velocity which is imposed to ensure that the field lines remain radial at the source surface ($r = 2.5\,R_\odot$). In a crude manner, this outflow velocity simulates the effect of the solar wind in opening coronal field lines, where $v_o = 100$ km s^{-1} is its peak value, and $r_w = 0.1\,R_\odot$ is its exponential fall-off length from the outer boundary. Note that the second term no longer affects the magnetic field, once the field lines become radial. Also, this term is negligible in the low closed-field corona.

To carry out the computations, positions within the domain are described in terms of new variables x, y, z such that $x = \phi$, $y = -\ln[\tan(\theta/2)]$ and $z = \ln(r/R_\odot)$ with a resolution of $\delta\phi$ (in heliographic degrees). For each of the cells, $h_\theta = h_\phi = r\sin\theta\delta\phi$ and $h_r = r\delta\phi$ in the vertical direction. To obtain second-order accuracy for the computations of $\mathbf{B} = \nabla \times \mathbf{A}$ and $\mathbf{j} = \nabla \times \mathbf{B}$, the vector potential $\mathbf{A}$, magnetic field $\mathbf{B}$, and current density $\mathbf{j}$ are defined on staggered grids: $\mathbf{A}$ and $\mathbf{j}$ are defined on the ribs of the cells while $\mathbf{B}$ is defined on the cell faces. The following boundary conditions are implemented:

1. The ϕ boundaries are periodic for all variables.
2. At latitudinal (θ) boundaries, $B_\theta = 0$, so that the field is tangential to the boundary. The electric current $\mathbf{j}$ is allowed to flow through the boundary so that the field lines may move within it.
3. At the outer radial boundary ($r = R_s$), the magnetic field $\mathbf{B}$ is assumed to be radial with the electric currents horizontal, so that the magneto-frictional method tends to remove all currents from open field lines.

Using these boundary conditions, either the entire sphere of the Sun or a localized volume may be considered. For the simulations presented here, the driving of the photospheric field and relaxation of the coronal field are carried out simultaneously. As a consequence, the coronal field never strictly satisfies the force-free condition but it departs from it by only a small amount. With this procedure, a sequence of coronal quasi-equilibrium states are produced.

2.2. Helicity Injection

The concept of magnetic helicity injection into the solar coronal field by small-scale vortical motions at the photosphere, and its condensation at the large-scale boundaries of unipolar regions to form filament channels, has been described by

Antiochos (2013). Detailed MHD simulations of this process, in which the vortical cells are well-resolved on the numerical grid and the transfer of helicity from small to large spatial scales by magnetic reconnection is represented, have been performed by Zhao et al. (2013). The simulations confirm the three-stage progression of (1) helicity injection at the small scales of the vortical convection, (2) helicity transfer via reconnection from the small injection scales to the large scales of the magnetically unipolar regions, and (3) helicity condensation at the perimeter of regions of unipolar magnetic field and vortical flow. On the Sun, those regions are bounded by PILs of the large-scale magnetic field, exactly where the strongly sheared filament channels form.

In the present work, the objective is to simulate the consequences of the helicity-condensation process, and its competition with other flux-transport processes that affect filament-channel formation, within a global-scale three-dimensional (3D) model. It would be very challenging to resolve flow fields that are the size of supergranules in such a calculation, and prohibitively expensive to resolve granules. Thus, we employ a spatially averaged, large-scale representation of the effects of helicity injection, transfer, and condensation in this paper. A derivation of the appropriate helicity injection term, which leads to Equation (3), is presented in the Appendix. A key feature of this model is that the total magnetic helicity injected by the vortical motions is conserved throughout the processes of reconnective transfer to, and condensation at, the largest scales. It is widely accepted that magnetic helicity is conserved during reconnection in all highly electrically conducting natural and laboratory plasmas (Taylor 1974, 1986; Berger 1984), including the solar corona. This property of rugged invariance also holds throughout the MHD simulations of helicity injection, transfer, and condensation reported by Zhao et al. (2013).

The average rate of injection of magnetic helicity into the large-scale coronal magnetic field, due to the small-scale vortical motions associated with the granular and supergranular convection cells, can be expressed simply through the source term

$$\mathbf{H}_{sg} = \begin{cases} \nabla_r(\zeta B_r), & r = R_\odot; \\ 0, & \text{otherwise.} \end{cases} \quad (4)$$

In this equation, ∇_r is the gradient operator including only the radial derivative, and ζ parameterizes the rate and scale of the helicity injection at the surface. The latter has the dimensions of a diffusivity and takes the explicit form

$$\zeta \equiv \overline{l^2 \omega_l}/2, \quad (5)$$

where l and ω_l are the radius and angular rotation rate, respectively, within the convection cells, and the overline denotes a spatial and temporal average over the characteristic scales of the convection. Note that this rotation rate, ω_l, is associated with a vortical flow of the cell in the plane of the photosphere, which gives rise to a radial component of the vorticity, $\nabla \times \mathbf{v}$. It is not the rotation rate of the cell across the surface of the Sun, nor is it a rotation rate of the cell associated with the strong central upwelling and annular downflows of the convection, which generate a horizontal component of $\nabla \times \mathbf{v}$. To avoid confusion, throughout the main body of this paper, we refer to ω_l simply as the vorticity of the convection cells, although the equivalence is strictly true only if the cells rotate rigidly, with ω_l independent of l throughout each cell. With respect to the relative contributions of the solar convection at different scales, note also that the supergranulation is anticipated to dominate strongly over the granulation, due to the size of the supergranules and the attendant much larger weighting of their l^2 factor to the effective diffusivity (Antiochos 2013).

Equations (4) and (5) for the helicity injection term are derived in the Appendix. They are employed in Equation (3) to calculate the consequences of the helicity injection for the evolution of the large-scale coronal magnetic field. Since the photospheric motions twist only the footpoints of the coronal magnetic field, the helicity injection term, $\mathbf{H}_{sg}$, is applied only at the first grid cell above the bottom boundary of the simulation domain. The effect of this term is to induce a horizontal twist component $\mathbf{B}_s$ of the magnetic field at the base of the corona wherever the product ζB_r is nonuniform across the surface (see the Appendix). The associated change in $\mathbf{B}$ in the global coronal model is divergence-free by construction. After being injected at the base, the twist component $\mathbf{B}_s$ then propagates upward along the field lines through the ideal convection term $\mathbf{v} \times \mathbf{B}$ in Equation (3). We note that, as a result of the staggered grid employed, B_r and ζB_r are defined at different locations: the product is positioned at the base of the radial ribs of the cells. Thus, a four-point average of the face values of B_r at the base of the corona is used to evaluate Equation (4), for inclusion in Equation (3).

Now, the supergranular helicity parameter, ζ, must be specified. It depends upon both l and ω_l, which can take on a range of values in the constantly shifting pattern of the supergranulation. The cell size l typically varies from 14,000 km to 30,000 km; for the simulations presented here, we simply assign a fixed, geometric-mean value $\bar{l} = 20{,}000$ km. At this time, neither the average vorticity of supergranules nor its spatial dependence versus latitude is firmly established from observations. The most compelling measurements come from applying time-distance and ring-diagram methods of helioseismology to global solar oscillations (Duvall & Gizon 2000; Gizon & Duvall 2003; Komm et al. 2007). These show that the vorticity at supergranular scales is positive (counterclockwise) in the downflow lanes between cells in the northern hemisphere and negative (clockwise) in those lanes in the southern hemisphere. The signs are reversed in the upwelling centers of the cells but the field dwells most of the time in the downflow lanes. This behavior of the signed vorticity is consistent with the influence of Coriolis forces on the convection. The vorticity magnitude is found to be on the order of 1×10^{-6} s^{-1}. In other observations, magnetograms and Dopplergrams in quiet-Sun regions have been analyzed to discover much more intense, but much smaller scale and very transient, cyclonic flows lacking any systematic dependence on latitude (Bonet et al. 2008, 2010; Zhang & Liu 2011). The relationship, if any, between these cyclonic flows and the supergranular convection is obscure. Additional observations are needed to fix more precisely the vorticity of the supergranular convection cells, whose value currently is at the limit of observational detection. Consequently, for simplicity in the present investigation, we consider only a spatially uniform value that falls in the range of $\overline{\omega_l} = 1\text{–}5 \times 10^{-6}$ s^{-1}. With this assumption, the helicity parameter ζ ranges from roughly 200 to 1000 km^2 s^{-1}, which is of the same order of magnitude as the surface diffusion coefficient, $D = 450$ km^2 s^{-1}.

As demonstrated below, one of the consequences of the supergranular helicity injection is to counter the effect of differential rotation. Thus, it is useful to compare the vorticity $\overline{\omega_l}$ to the differential-rotation gradient, $\omega_{dr} \equiv d\Omega/d\theta$. The latter is shown in Figure 1 as a function of latitude λ,

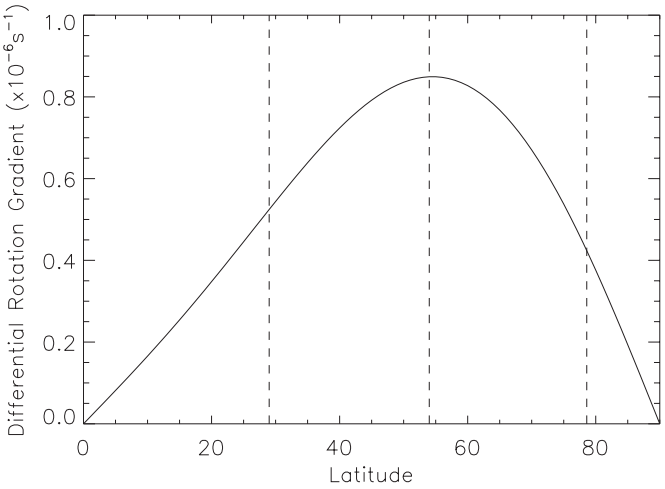

Figure 1. Differential-rotation gradient, $\omega_{dr} \equiv d\Omega/d\theta$, vs. latitude. Vertical dashed lines indicate the latitudes of the polarity inversion line in the axisymmetric cases described in Section 4.

in the northern hemisphere only, since the profile is symmetric about the equator. From the graph, it can be seen that the gradient of differential rotation peaks at $\lambda = 54^\circ$, at a rate $\omega_{dr} = 0.85 \times 10^{-6}$ s^{-1}. This peak value is, therefore, just slightly lower than the smallest nonzero value of supergranular vorticity ($\overline{\omega_l} = 1 \times 10^{-6}$ s^{-1}) considered in this paper. The vertical dashed lines denote the latitudes of the east–west PILs for the simulations discussed in Section 4. It should be noted that, for the PILs at $\lambda = 29^\circ$ and 79°, the lowest imposed vorticity is nearly twice as high as the differential-rotation gradient.

To investigate the effects of the supergranular helicity injection, three distinct sets of simulations were carried out. In Section 3, a single, isolated bipole is considered. Following this, in Section 4, the competing effects of differential rotation and the supergranular helicity injection are considered for an east–west PIL. Finally, in Section 5, simulations of the interaction of a single bipole with a polar field are considered during both the rising and declining phases of the solar cycle. In all of the simulations, the initial coronal field is constructed using the potential-field/source-surface approximation, in which the field lines are required to assume a radial orientation at and beyond $r = 2.5\ R_\odot$. As a result, the initial configurations contain a mixture of open and closed field lines.

3. BIPOLE AT 25° LATITUDE

To investigate the role of supergranular helicity injection, its effect on a single magnetic bipole is first considered. The initial condition is shown in Figure 2(a), where the thin black lines denote the limb of the Sun and the limits of the computational domain. The domain extends over $\phi \in [0^\circ, 120^\circ]$, $\lambda \in [-5^\circ, +55^\circ]$, and $r \in [1\ R_\odot, 2.5\ R_\odot]$ with a resolution of $241 \times 143 \times 106$ grid points. The bipole is placed at 25° latitude in the northern hemisphere. Red and blue contours represent positive and negative magnetic flux, respectively, while the thick black lines follow the magnetic field. The bipole is placed so that both polarities lie at the same latitude. Thus, the PIL dividing the two polarities initially lies in the north–south direction.

The effect of the helicity injection term can be seen in Figures 3(a) and (c), where the coronal field is shown after 27 and 54 days, respectively, of supergranular helicity injection with a vorticity of $\overline{\omega_l} = 1 \times 10^{-6}$ s^{-1}. Since no differential rotation, meridional flow, or surface diffusion is applied, the

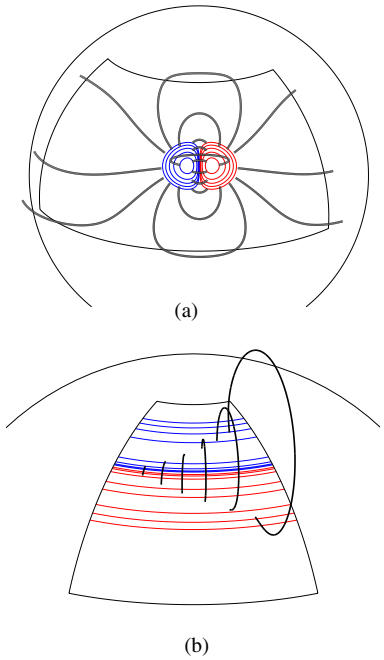

Figure 2. Initial conditions for (a) an isolated bipole at 25° latitude and (b) an east–west PIL at 54° latitude. Red/blue contours represent positive/negative flux; thick black lines are field lines; thin black lines demarcate the boundaries of the computational domain and the limb of the Sun.

(A color version of this figure is available in the online journal.)

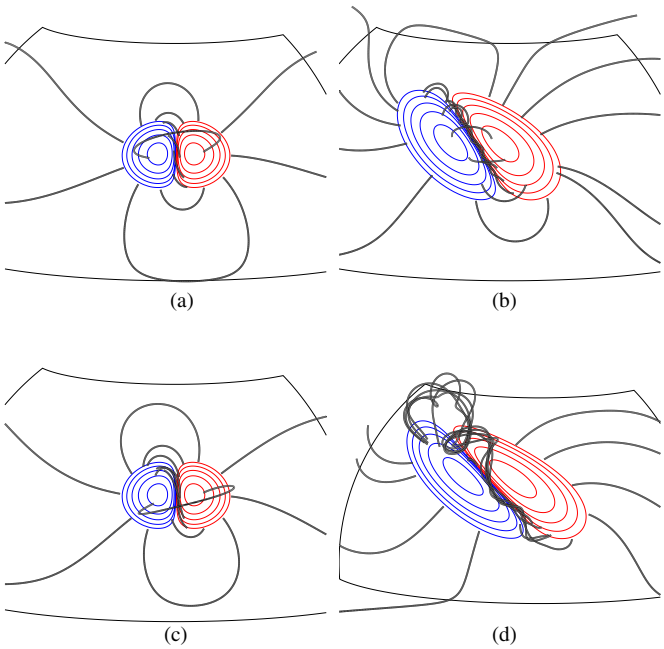

Figure 3. Evolution of an isolated bipole when (left column) helicity injection with vorticity $\overline{\omega_l} = 1 \times 10^{-6}$ s^{-1} is applied with no other surface flux-transport processes, and (right column) surface flux transport is applied with no helicity injection. Elapsed times are 27 days (top row) and 54 days (bottom row). Line styles are the same as in Figure 2.

(A color version of this figure is available in the online journal.)

radial field component at the photosphere remains fixed over the time period of the simulation. The positive vorticity injects a negative helicity into the field lines lying at low heights above the PIL. As a result, a dextral skew of the field develops. This skew is seen as a sheared arcade on day 27 and a flux rope on day 54. The

formation of the flux rope is due to numerical diffusion, as once the coronal field overlying the PIL becomes strongly sheared, reconnection occurs in the corona. From this, it is clear that the supergranular helicity injection term produces a chirality of the field that is consistent with the dominant hemispheric pattern of filaments.

While this is true, it should be noted that if surface flux-transport effects alone are applied over the same time period, then a dextral chirality is also found along the PIL between the two polarities of the bipoles. This can be seen in Figures 3(b) and (d), which show that simulation after 27 and 54 days of evolution. Due to the application of surface flux-transport processes, the radial field at the photosphere no longer remains fixed. The east–west shearing of the bipole due to differential rotation is clearly evident, along with the poleward advection due to meridional flow and expansion due to surface diffusion. In addition, there is cancellation of flux at the PIL. As the field lines initially lie east–west, with their footpoints at the same latitude, their orientation is not affected by differential rotation. In contrast, the PIL is rotated counter-clockwise, and this builds up a dextral skew. Flux cancellation aids this process, so that a stronger shearing of the field and a larger flux-rope structure is produced earlier in the simulation than for the case with helicity injection only. After 54 days, the flux rope has become so large that it can no longer be held down by the overlying arcades, and it starts to rise. This removes a large amount of shear from the field overlying the PIL but still leaves behind a dominant dextral skew.

Along the north–south PIL of the bipole, seen in Figure 3, the supergranular helicity injection term with positive vorticity and surface flux-transport processes have the same basic effects but act on different timescales. Flux transport develops shear in the field faster. This result may seem surprising, as the gradient of differential rotation is less than the applied supergranular vorticity. However, the extra effect of surface diffusion speeds up the process of shearing the field, as it diffuses flux toward the PIL and reduces the footpoint separation of already sheared field lines.

In Figure 4, diagnostic tests of the supergranular helicity injection term can be seen in graphs of (a) normalized volume integrated magnetic energy and (b) relative magnetic helicity. In each case, the quantities are graphed versus the number of days elapsed in the simulation. The magnetic energy,

$$E_m = \int_V B^2 d\tau, \tag{6}$$

is normalized to its initial value, which is the same for all simulations. The relative magnetic helicity is calculated using the formula of Finn & Antonsen (1985),

$$H_r = \int_V (\mathbf{A} + \mathbf{A_p}) \cdot (\mathbf{B} - \mathbf{B_p}) d\tau, \tag{7}$$

where $\mathbf{A_p}$ and $\mathbf{B_p} = \nabla \times \mathbf{A_p}$ represent the potential field that possesses the same normal magnetic field components on all boundaries as the actual field.

Each of the graphs compares four simulations representing different physical effects and parameter values. The effect of the radial outflow velocity when no surface motions or supergranular helicity injection is applied is quantified by the dashed line. The other three lines demonstrate the radial outflow velocity combined with flux-transport processes alone (solid line) and with helicity injection alone (fixed radial field at the photosphere) for vorticities of 1×10^{-6} s^{-1} (dotted) and 5×10^{-6} s^{-1} (triple-dot-dashed). From Figure 4, it is clear that the radial outflow velocity has no significant effect on the magnetic energy and relative helicity.

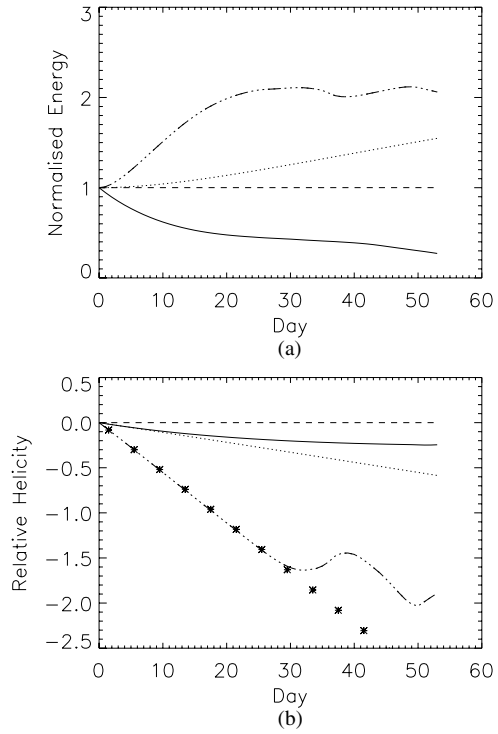

Figure 4. Normalized (a) magnetic energy E_m (Equation (6)) and (b) relative magnetic helicity H_r (Equation (7)) vs. day of simulation for an isolated bipole. In all simulations, a radial outflow is applied at the upper boundary. The various line styles denote: no photospheric boundary transport (dashed); helicity injection at a rate of $\overline{\omega_l} = 1 \times 10^{-6}$ s^{-1} (dotted) or $\overline{\omega_l} = 5 \times 10^{-6}$ s^{-1} (triple-dot-dashed); and standard surface flux transport without helicity injection (solid). In (b), the stars denote the results for a helicity injection rate of $\overline{\omega_l} = 1 \times 10^{-6}$ s^{-1}, scaled up by a factor of 5.

For the case where only flux transport is included, the total magnetic energy is continually decreasing due to flux cancellation. In contrast, when supergranular helicity injection is considered, the magnetic energy increases. A nearly linear increase is found when $\overline{\omega_l} = 1 \times 10^{-6}$ s^{-1}. However, for the case of $\overline{\omega_l} = 5 \times 10^{-6}$ s^{-1}, the magnetic energy eventually levels off at approximately twice the original value.

For both the flux-transport case (solid line) and the two cases with helicity injection (dotted, triple-dot-dashed), the relative magnetic helicity is always negative. The flux-transport results are consistent with the results of DeVore (2000), who showed that, when differential rotation acts on an east–west oriented bipole, a negative helicity injection occurs during the early stages of evolution. This negative injection then slows down as the bipole becomes oriented in a north–south direction. When the supergranular helicity injection is included with vorticity $\overline{\omega_l} = 1 \times 10^{-6}$ s^{-1}, the relative helicity shows a linear trend, which is expected when the radial field component is held fixed. In contrast, when the vorticity is increased to $\overline{\omega_l} = 5 \times 10^{-6}$ s^{-1}, it is linear only up until day 30. Beyond this point, the relative helicity increases for a time before once again decreasing linearly. The changing trend of relative helicity is the result of a flux rope forming above the internal PIL of the bipole. Eventually, it becomes too strong to be held down by the overlying arcade and subsequently is ejected through the top boundary. The increase in relative helicity at that time is due to

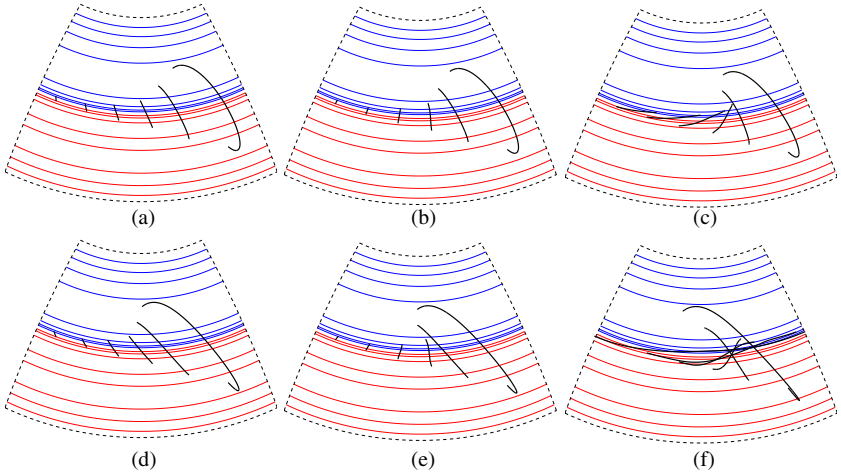

Figure 5. Competing effects of differential rotation and helicity injection (no surface diffusion). Results are shown for differential rotation alone (left column) and for differential rotation plus helicity injection at rates of $\overline{\omega_l} = 1 \times 10^{-6}$ s^{-1} (middle column) and $\overline{\omega_l} = 5 \times 10^{-6}$ s^{-1} (right column). Elapsed times are 10 days (top row) and 20 days (bottom row). Dashed lines indicate where the computational domain is truncated in the images; other line styles are the same as in Figure 2.

(A color version of this figure is available in the online journal.)

the loss of negative helicity by the ejection, not to any injection of positive helicity. Following the ejection, the previous linear trend with similar slope resumes until a second ejection occurs at around day 50. The stars in Figure 4(b) denote the results from the simulation with a vorticity of $\overline{\omega_l} = 1 \times 10^{-6}$ s^{-1} multiplied by a factor of 5. These show good agreement with the results from the simulation with vorticity $\overline{\omega_l} = 5 \times 10^{-6}$ s^{-1} up to the time when the first ejection occurs.

4. EAST–WEST PIL AT 54° LATITUDE

The next series of simulations compares the competing effects of differential rotation and supergranular helicity injection when the PIL lies in an east–west direction, as is shown in Figure 2(b). This axisymmetric flux distribution is typical of a high-latitude east–west polar or subpolar crown PIL and filament channel. For the case shown, the PIL lies at 54° latitude, while the computational domain extends over $\phi \in [0°, 60°]$, $\lambda \in [25°, 75°]$, and $r \in [1\ R_\odot, 2.5\ R_\odot]$, with a resolution of $101 \times 149 \times 88$ grid points. In the initial configuration, a series of field lines (thick black lines) extending over a range of latitudes and heights is shown.

Figure 5 illustrates the competing effects of differential rotation and supergranular helicity injection alone, with meridional flow and supergranular diffusion excluded. The top and bottom rows show the results after 10 and 20 days of simulation, respectively. As differential rotation is independent of ϕ, the contours of B_r at the photosphere remain unchanged and the footpoints of the field lines are simply advected along the contours in all cases. In Figures 5(a) and (d), the effect of applying differential rotation alone is considered. It can be clearly seen that over the 20 day period, differential rotation shears the field lines in an east–west direction and builds up a sinistral skew. This is inconsistent with the dominant (dextral) chirality found for northern hemisphere filaments.

In Figures 5(b) and (e), results are shown when both differential rotation and supergranular helicity injection are included, where the helicity injection occurs with a vorticity of 1×10^{-6} s^{-1}. The positive value of vorticity injects a negative helicity, which is opposite in sign to the helicity injected by the differential rotation. With the inclusion of the supergranular helicity injection, the short field lines that lie at low heights now remain unskewed after 10 days but begin to develop a slight dextral skew after 20 days. This is consistent with the vorticity being slightly greater than the local differential-rotation gradient. Therefore, locally around the PIL the supergranular helicity injection has countered and overcome the effect of differential rotation, to give a chirality consistent with the dominant hemispheric pattern. While this occurs near the PIL, for field lines with footpoints far away from the PIL the effect of differential rotation still dominates and a sinistral skew develops. Finally, in Figures 5(c) and (f), results can be seen when the vorticity is increased to $\overline{\omega_l} = 5 \times 10^{-6}$ s^{-1}. Due to the increased negative helicity injection, a strong dextral skew develops on the short, low-lying field lines after just 10 days. After 20 days, a strong dextral axial field lies along the full length of the PIL. While this strong axial field exists at low heights, differential rotation still dominates for high-lying field lines that have a large latitudinal separation in their footpoints. This means that the skew of the field reverses with height, and a negative-helicity region lies beneath a larger-scale positive-helicity region.

In Figure 6(a), the skew angle of the field lines above the PIL can be seen as a function of height, up to 1.2 $R_\odot$, after 20 days of evolution. The skew angle γ is defined as

$$\cos\gamma = \frac{\mathbf{B}_h \cdot \hat{\mathbf{n}}}{\mid \mathbf{B}_h \mid\mid \hat{\mathbf{n}} \mid}, \tag{8}$$

where $\mathbf{B}_h$ is the horizontal field at any given height above the PIL and $\hat{\mathbf{n}} = -\nabla B_r / \mid \nabla B_r \mid$ is the unit normal over the PIL at $r = 1\ R_\odot$, pointing from positive to negative flux. Dextral skew is defined when $\gamma > 0°$, and sinistral skew is defined when $\gamma < 0°$. If $\mid \gamma \mid < 90°$, the field has normal polarity and takes the form of an arcade. In contrast, if $\mid \gamma \mid > 90°$, the field has inverse polarity and is dipped. From the graph, it can be seen that when differential rotation alone is applied (solid line), then γ is always negative and a sinistral chirality is produced; however, the skew is generally weak. In contrast, when the supergranular helicity injection term is included with a vorticity of $\overline{\omega_l} = 1 \times 10^{-6}$ s^{-1} (dotted), 2.5×10^{-6} s^{-1} (dash-dotted), or 5×10^{-6} s^{-1} (triple-dot-dashed), then a dextral skew is found at low heights. However, only for the two higher values of vorticity does a clear region of dextral skew extend to substantial heights.

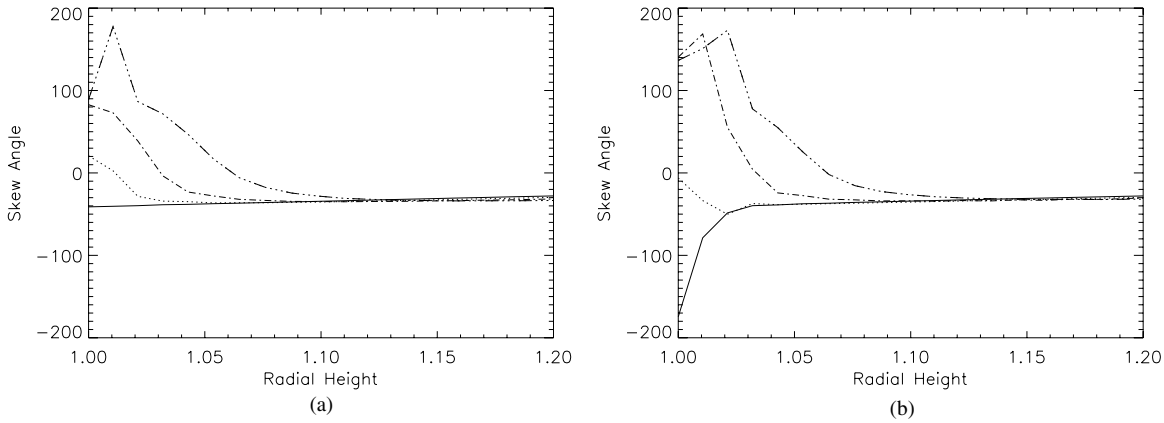

Figure 6. Skew angle γ vs. radial height after 20 days, for the cases of (a) differential rotation and supergranular helicity injection only and (b) in combination with surface diffusion. The various line styles denote different rates of helicity injection: $\overline{\omega_l} = 0\ s^{-1}$ (solid), $\overline{\omega_l} = 1 \times 10^{-6}\ s^{-1}$ (dotted), $\overline{\omega_l} = 2.5 \times 10^{-6}\ s^{-1}$ (dash-dotted), and $\overline{\omega_l} = 5 \times 10^{-6}\ s^{-1}$ (triple-dot-dashed). Positive values indicate a dextral skew; negative values indicate a sinistral skew.

When $\overline{\omega_l} = 5 \times 10^{-6}\ s^{-1}$, a flux-rope structure forms as can be seen in Figure 5(f).

Figure 7 shows the same cases as Figure 5 but now with the nonlocal effect of surface diffusion included. Due to the inclusion of surface diffusion, the normal component B_r diffuses across the solar surface both toward the PIL, where cancellation occurs, and away from it. The cancellation of flux at the PIL has a significant effect on the chirality produced. For the case of differential rotation without supergranular helicity injection (Figures 7(a) and (d)), the inclusion of surface diffusion results in the development of a strong sinistral skew after 20 days. The stronger skew occurs as a result of surface diffusion converging footpoints toward the PIL, which decreases their latitudinal separation and increases the skew. Hence, while the nonlocal effect of surface diffusion cannot create skew by itself, it can enhance the skew added by differential rotation. When supergranular helicity injection with vorticity $\overline{\omega_l} = 1 \times 10^{-6}\ s^{-1}$ is included (Figures 7(b) and (e)), different results are obtained compared to Figures 5(b) and (e). Now, a weak sinistral skew is found at low heights all along the PIL, where before some of the skew was dextral. The changing orientation of the skew, compared to that found previously, occurs as supergranular helicity injection can only dominate over differential rotation locally at the PIL. Once these field lines have been cancelled, longer field lines where differential rotation dominates are advected toward the PIL. As these field lines already have a sinistral skew that is further enhanced by the convergence due to surface diffusion, the supergranular helicity injection is unable to overcome these combined effects. Nevertheless, the helicity injection does limit the skew and stops a strong sinistral axial field from forming. Finally, in Figures 7(c) and (f), results can be seen when the supergranular vorticity is increased to $\overline{\omega_l} = 5 \times 10^{-6}\ s^{-1}$. With the increased value of vorticity, the effect of differential rotation can once again be overcome, and a dextral axial field component is produced at low heights over the PIL. On comparing Figure 7(f) to Figure 5(f), it can be seen that the inclusion of surface diffusion makes the axial field much stronger than before. This illustrates a key feature of surface diffusion: it always enhances the existing skew, irrespective of whether it is dextral or sinistral. Therefore, for the supergranular helicity injection to dominate over differential rotation and produce a dextral skew, it must be sufficiently strong to overcome differential rotation not just locally at the PIL but in an extended zone around it. As a consequence of nonlocal effects, to overcome differential rotation, the vorticity must be roughly a factor of 2–3 higher than the local differential-rotation gradient. This can be seen in Figure 6(b), where in each case, the skew is significantly enhanced compared to that found before (Figure 6(a)), except for $\overline{\omega_l} = 1 \times 10^{-6}\ s^{-1}$, which is of opposite sign.

Finally, Figure 8 shows the relative magnetic helicity for the simulations in which only differential rotation and supergranular helicity injection are included. In all cases, the curves are positive, indicating that over the full computational domain, the injection of positive helicity by differential rotation is dominant. However, as the rate of supergranular helicity injection increases, lower positive values are obtained, reflecting the larger injection of negative helicity.

The results above illustrate a key feature that must be taken into account: due to the nonlocal process of surface diffusion converging fields toward the PIL, it is insufficient for the supergranular helicity injection to dominate over differential rotation only locally. Rather, it must dominate nonlocally as well and be sufficiently higher than the local rate of differential rotation to have a dominant effect. While the results above have been shown for a PIL at 54° latitude, similar results were found for PILs at 29° and 79° latitude, in the critical vorticity values needed relative to the local rates of differential rotation.

5. BIPOLE PLUS POLAR FIELD

In this section, we consider magnetic field configurations that can occur in both the rising and declining phases of the solar cycle.

5.1. Rising Phase

Results are first shown for the interaction of a single magnetic bipole with the polar field, for a magnetic configuration that is representative of the rising phase of the solar cycle. The initial configuration can be seen in Figure 9(a), where the bipole is centered at a latitude of 20° and has a tilt angle of 0°. The computational domain extends over $\phi \in [0°,140°]$, $\lambda \in [-4.5°, +65°]$, and $r \in [1\ R_\odot, 2.5\ R_\odot]$, with a resolution of $281 \times 183 \times 106$ grid points. As the magnetic configuration represents the rising phase of the solar cycle, the polar field has the same polarity as that of the lead polarity of the bipole. Correspondingly, the PIL wraps around the following polarity and in the initial configuration the PIL may be regarded as consisting of two distinct parts. First, there is the north–south

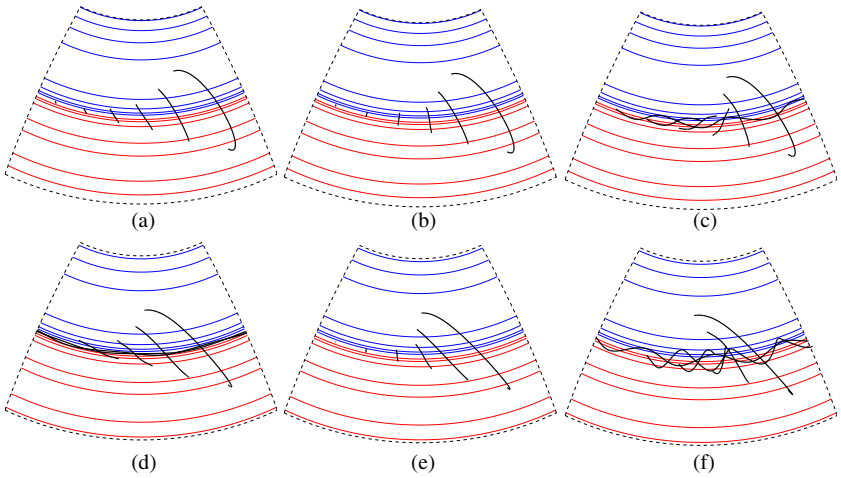

Figure 7. Competing effects of differential rotation and supergranular helicity injection with surface diffusion included. The plots show the results for differential rotation and surface diffusion only (left column), with helicity injected at a rate of $\overline{\omega_l} = 1 \times 10^{-6}$ s^{-1} (middle column), and with helicity injected at a rate of $\overline{\omega_l} = 5 \times 10^{-6}$ s^{-1} (right column). Elapsed times are 10 days (top row) and 20 days (bottom row). Line styles are the same as in Figure 5.

(A color version of this figure is available in the online journal.)

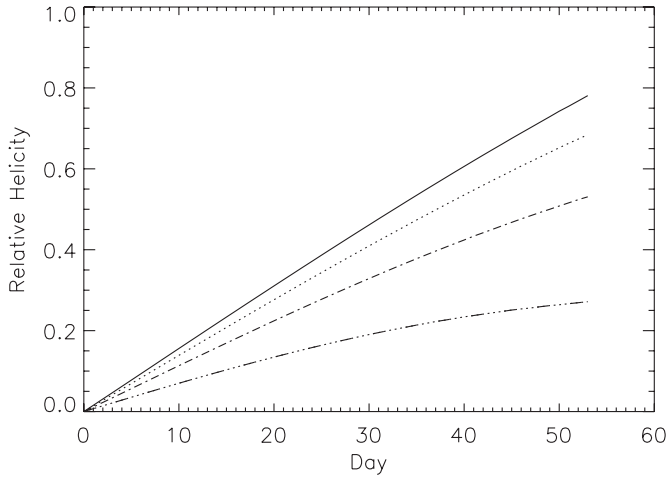

Figure 8. Relative magnetic helicity H_r for simulations with an east–west PIL at 54° latitude when differential rotation and helicity injection only are applied (no surface diffusion). The various line styles denote different rates of helicity injection: $\overline{\omega_l} = 0$ s^{-1} (solid), $\overline{\omega_l} = 1 \times 10^{-6}$ s^{-1} (dotted), $\overline{\omega_l} = 2.5 \times 10^{-6}$ s^{-1} (dash-dotted), and $\overline{\omega_l} = 5 \times 10^{-6}$ s^{-1} (triple-dot-dashed).

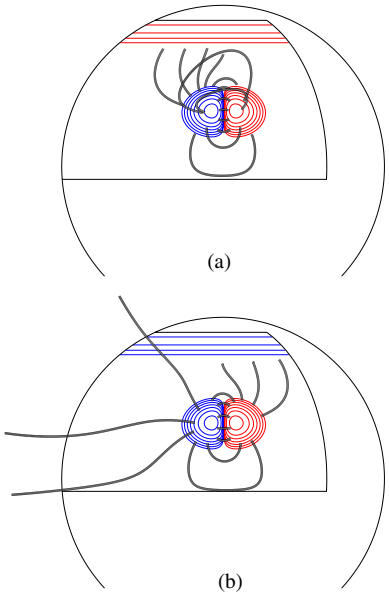

Figure 9. Initial conditions for a single bipole at 20° latitude in the (a) rising and (b) declining phases of the solar cycle. Line styles are the same as in Figure 2.

(A color version of this figure is available in the online journal.)

part of the PIL that separates the two polarities of the bipole, above which the field lines have an initial east–west orientation. Second, the PIL wraps around the top of the following polarity, where it separates the following polarity from the polar field. Here, the PIL has an east–west orientation, with the field lines lying north–south. Therefore, the initial configuration features both orientations of the PIL and the field lines that have been considered previously.

In Figure 10, the results after 27 days of evolution for full surface flux transport (a) alone and (b) combined with supergranular helicity injection (with vorticity $\overline{\omega_l} = 1 \times 10^{-6}$ s^{-1}) can be seen. As the helicity injection does not affect B_r, the surface magnetic field configuration is identical in the two cases. During the evolution, differential rotation rotates the north–south part of the PIL toward an east–west orientation, so that it becomes more aligned with the higher latitude east–west part of the PIL. Therefore, over time, the two parts of the PIL increasingly become less distinct.

For the case of surface flux-transport effects alone (Figure 10(a)), a dextral axial field and flux-rope structure form along the mainly north–south part of the PIL. The formation process is the same as that discussed in Section 3. On the other hand, a slight sinistral skew forms along the small east–west high-latitude PIL. For the case where supergranular helicity injection is included (Figure 10(b)), very similar results are found. The only differences are that the dextral flux-rope structure forms faster along the north–south PIL, and the sinistral skew found on the east–west PIL is slightly weaker. Thus, while the helicity injection does have an effect, it mainly changes the timescales for the formation of the axial field. To determine whether such an effect occurs on the Sun, detailed observations of the timescale to develop sheared fields is required. Both simulations described above have been run for a further three rotations, and similar results are found. Only in the later stages of the simulation, when

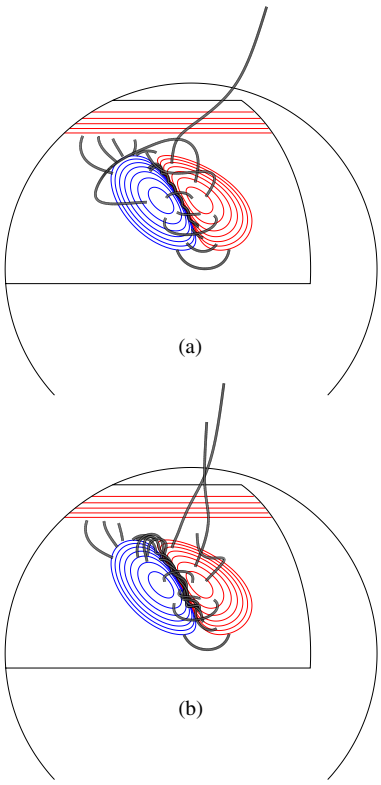

Figure 10. Interaction of a single magnetic bipole at 20° latitude with the polar field in the rising phase of the solar cycle for full surface flux transport (a) alone and (b) with helicity injection at a rate of $\overline{\omega_l} = 1 \times 10^{-6}$ s^{-1}. The elapsed time is 27 days. Line styles are the same as in Figure 2.

(A color version of this figure is available in the online journal.)

the initial north–south PIL has rotated to lie east–west, does a sinistral axial component form along the whole PIL, consistent with the results of Section 4.

5.2. Declining Phase

The initial condition for the simulations that represent the declining phase of the solar cycle can be seen in Figure 9(b). As for the rising phase, the bipole is placed at 20° latitude and has a tilt angle of 0°. The key difference is that now the polar field is of opposite sign to that of the lead polarity of the bipole. This means that the PIL follows a different path and forms what is known as a switchback. Again, there is a north–south portion of the PIL that separates the two polarities, called the "return arm". The east–west portion that lies at near constant latitude is called the "lead arm". As the lead arm lies at constant latitude, it is unaffected by differential rotation. In contrast, the return arm is rotated by differential rotation to have an east–west component. Although the return arm develops an east–west component, the lead and return arms do not merge into one PIL and remain distinct from one another throughout the entire simulation period.

The results of the simulations can be seen in Figure 11, where the simulation is run for 90 days. The first column considers only flux transport processes for (a) 30 days, (d) 60 days, and (g) 90 days. Consistent with the previous simulations, a dextral skew develops along the return arm. The amount of skew varies as first a dextral flux rope forms (day 30), then starts to rise and is ejected from the simulation (days 60–70), and finally begins to reform again (day 90). In contrast, on the lead arm, a sinistral skew develops as differential rotation shears the field lines that lie north–south. In the later stages of the evolution, a sinistral flux rope forms as flux cancellation takes place between the lead polarity of the bipole and the polar field. A large flux rope of sinistral skew can be seen in Figure 11(g). Therefore, the chirality along the lead arm is inconsistent with the dominant chirality pattern found for northern-hemisphere filaments.

The second column in Figure 11 considers the effect of the supergranular helicity injection when the vorticity is 1×10^{-6} s^{-1}. With this additional helicity injection, the dextral axial component strengthens along the return arm and the flux rope forms earlier and is correspondingly larger at each of the times shown in the figure. Along the lead arm, a sinistral skew still develops, although by comparing the first and second columns, it can be seen that at each time, the sinistral skew is now weaker. The negative helicity injection driven by the positive vorticity of the supergranular cells is, however, insufficient to overcome the positive helicity injection due to differential rotation.

In the third column of Figure 11, the effect of increasing the vorticity to $\overline{\omega_l} = 5 \times 10^{-6}$ s^{-1} can be seen for the same times. Along the lead arm, slightly different results are found. On both day 30 and day 60, the sinistral skew is much weaker than before. The higher rate of helicity that is injected by the increased value of supergranular vorticity can now overcome the positive helicity injection by differential rotation, and the field lines become twisted in the opposite sense. While this is true for days 30 and 60, a more dominant sinistral skew can be seen by day 90, as longer field lines that previously have been more strongly sheared by differential rotation converge toward the PIL. Thus, when the larger vorticity is applied, the supergranular helicity injection can help to minimize the production of sinistral skew over time along the lead arm. While it does not produce dextral skew on the lead arm, by minimizing the sinistral skew, it does allow an overall preferred dextral pattern to form along the entire length of the PIL, due to the consistent production of dextral skew along the return arm in all of the cases.

Finally, in Figure 12, another simulation of the declining phase can be seen, where this time the central location of the bipole is placed at 30° latitude with a tilt angle of 0°. The north–south field lines that lie above the lead arm are now much shorter. As before, field configurations are shown after (a) 30 days, (b) 60 days, and finally (c) 90 days of evolution, with a vorticity of $\overline{\omega_l} = 5 \times 10^{-6}$ s^{-1}. With the shorter field lines, the rate of helicity injection can now overcome the nonlocal effects of differential rotation and supergranular diffusion to produce a dextral skew along the lead arm. After 90 days, a clear dextral axial component with a flux rope that bends around from the return to the lead arms can be seen. The results clearly show that, as long as the initial field lines upon which supergranular helicity injection acts are short in length, then the injection can overcome the effect of differential rotation if a sufficiently large vorticity is applied. Even if the value of vorticity is not sufficient to produce dextral skew on the lead arm, so long as it can minimize the effect of differential rotation producing sinistral skew on the lead arm, it will allow a dominant dextral pattern to form over the region as a whole, as both differential rotation and supergranular helicity injection produce a dextral pattern on the return arm. This indicates that return arms are preferred sites for the location of negative helicity and dextral skew, which in principle may be tested observationally.

6. DISCUSSION AND CONCLUSIONS

Antiochos (2013) proposed the concept of helicity condensation acting in the solar chromosphere and corona. Within this

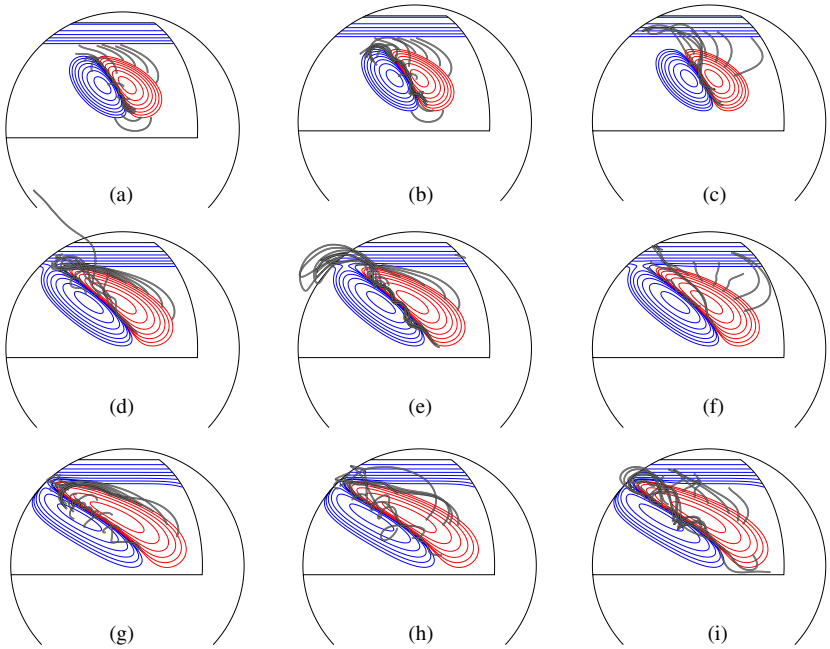

Figure 11. Interaction of a single magnetic bipole at 20° latitude with the polar field in the declining phase of the solar cycle. Results are shown for full surface flux transport alone (left column) and in combination with supergranular helicity injection at rates of $\overline{\omega_I} = 1 \times 10^{-6}$ s^{-1} (middle column) and $\overline{\omega_I} = 5 \times 10^{-6}$ s^{-1} (right column). The elapsed times are 30 days (top row), 60 days (middle row), and 90 days (bottom row). Line styles are the same as in Figure 2.

(A color version of this figure is available in the online journal.)

model, magnetic helicity first arises as a consequence of vortical motions in small-scale convective cells. It is then redistributed across the surface of the Sun, through the process of magnetic reconnection, to lie above or condense along large-scale PILs. Assuming that the vortical motions are predominantly counterclockwise in the northern hemisphere and clockwise in the southern, in the observed sense of differential rotation, then these motions result in a negative/positive magnetic helicity injection in the northern/southern hemisphere. The sign of injection is consistent with the dominant hemispheric pattern of filament chirality, where dextral/sinistral filaments containing negative/positive helicity dominate in the northern/southern hemisphere. The present paper considers this new method of helicity injection and condensation within the context of large-scale magnetic flux-transport simulations and global-scale modeling of the coronal magnetic field.

Previous models that have considered the origin of the hemispheric pattern of solar filaments have focused solely on large-scale mechanisms for injecting magnetic helicity into the corona. The first mechanism considered, differential rotation, injects both positive and negative magnetic helicity into each hemisphere, depending on the orientation of the PIL. On a north–south PIL, negative/positive helicity is injected in the northern/southern hemisphere, which matches the hemispheric pattern of filaments. In contrast, on an east–west PIL, as occurs at high latitudes, the sign of helicity injection is reversed in each hemisphere. Note also that differential rotation, alone, does not produce a concentration of shear at a PIL as is observed in actual filament channels. A further mechanism, flux cancellation (surface diffusion), is needed in order to match the observations.

The second mechanism of helicity injection considered is associated with the emergence of new magnetic bipoles. The bipoles are specified to have an internal magnetic helicity that matches the observations of Pevtsov et al. (1995), namely, negative/positive in the northern/southern hemisphere. Through including these two large-scale methods of helicity injection, Yeates et al. (2008) found a 96% agreement between the observed chirality of filaments and the chirality produced by the model over a six-month period (see Yeates & Mackay 2009a). An important aspect of the agreement was that it was equally good for both the majority and minority chirality filaments in each hemisphere. While an excellent agreement was obtained, one limitation of the study was that it only considered filaments below 60° latitude. In a further study, Yeates & Mackay (2012) simulated the entire length of cycle 23 and showed that, in the rising phase of the cycle, these two effects can produce the correct sign of helicity and chirality to match filament observations at high latitudes. In contrast, the opposite was found for the declining phase, where positive helicity was dominant at high latitudes in the northern hemisphere and negative helicity in the southern hemisphere. It should be noted that no detailed observational studies of filament chirality have been carried out so far in the declining phase of the solar cycle.

One limitation of the injection of magnetic helicity into the solar corona through the emergence of new bipoles is that it occurs only sporadically and at low latitudes. As flux is transported poleward and eruptions occur, this magnetic helicity can be lost. Once lost, the correct sign of helicity to produce the observed hemispheric pattern cannot always be regenerated in situ. Consequently, the helicity-condensation model put forward by Antiochos (2013) provides an attractive third source of helicity injection. A key feature of this model is that it acts over all latitudes, at all times, and can regenerate magnetic helicity in situ, even after eruptions. Furthermore, it is not sensitive to the orientation of the PIL, so that the same sense of shear will form all along a single PIL irrespective of whether it contains a switchback. Therefore, the present paper has considered this new method of helicity injection and concentration within the context of large-scale magnetic flux-transport simulations. For simplicity, we have only carried out simulations in the northern

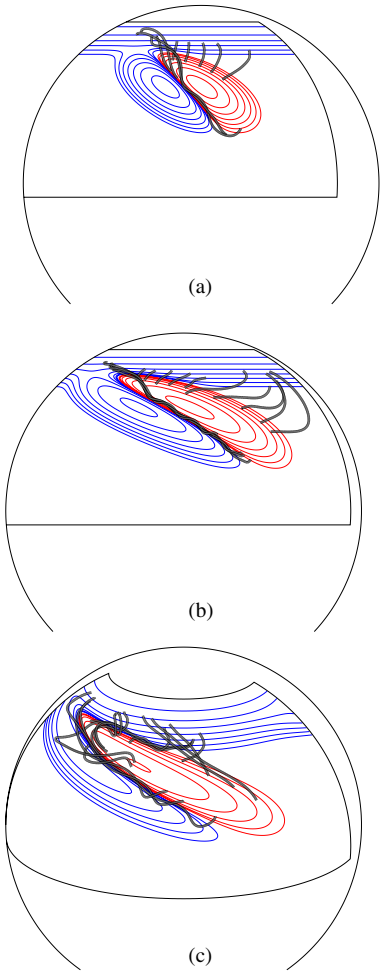

Figure 12. Interaction of a single magnetic bipole at 30° latitude with the polar field in the declining phase of the solar cycle. Results are shown for full surface flux transport with supergranular helicity injection at a rate of $\overline{\omega_l} = 5 \times 10^{-6}$ s^{-1}. Elapsed times are (a) 30 days, (b) 60 days, and (c) 90 days. Line styles are the same as in Figure 2.

(A color version of this figure is available in the online journal.)

hemisphere and so assumed a counter-clockwise (positive) vorticity for the small-scale convective motions. While the results are presented with regard to the northern hemisphere, the converse is true for the south.

To implement the small-scale injection of magnetic helicity, we developed a large-scale averaged representation of the small-scale dynamics (see the Appendix). Within this formulation, two key parameters arise: l, the cell size, and $\overline{\omega_l}$, the cell vorticity. Each of these parameters currently exhibits a high degree of uncertainty, including the magnitude of each term and its variation with latitude. For simplicity, we have assumed typical values of $\bar{l} = 20{,}000$ km and $\overline{\omega_l} = 1$–5×10^{-6} s^{-1}, and only considered helicity injection from supergranular cells. The lowest value of the vorticity is slightly larger than the peak value of the differential-rotation gradient, $\omega_{dr} = 0.85 \times 10^{-6}$ s^{-1}, which occurs at $\lambda = 54°$. The two helicity injection parameters combine to form the helicity injection coefficient $\zeta \equiv \overline{l^2 \omega_l}/2$, which ranges from roughly 200 to 1000 km^2 s^{-1}.

To quantify the effect of helicity injection due to vortical motions in supergranular cells, a variety of magnetic field configurations typical of those found on the Sun have been considered. These include high-latitude east–west-oriented polar crown or subpolar crown PILs and the interaction of a magnetic bipole with the polar field for both the rising and declining phases of the solar cycle. These simulations show two key features: (1) for a north–south oriented PIL in either the rising or declining phase of the cycle, both differential rotation and supergranular helicity injection introduce the same sign of helicity. In each hemisphere, this helicity matches that required to reproduce the hemispheric pattern of filaments. Therefore, at such locations, the two mechanisms are complementary. (2) Along an east–west oriented PIL, such as that of the polar crown or subpolar crown, the vorticity of the supergranular helicity injection must be roughly 2–3 times higher than the local value of the differential-rotation gradient to overcome the sign of helicity injection from differential rotation. This factor of 2–3 is required so that the supergranular helicity injection can overcome differential rotation not just locally at the PIL but also in an extended zone around it. This is necessary because surface diffusion converges field lines with a large latitudinal separation in their footpoints toward the PIL. The latitudinal separation in footpoints means that the field lines experience a larger rate of differential rotation than that found locally at the PIL.

The most important aspect of the helicity injection from supergranular cells occurs when considering the interaction of a bipole with the polar field in the declining phase of the cycle. In some instances, the helicity injection can overcome differential rotation along the so-called east–west lead arm but not in all cases. So long as the field lines overlying the lead arm are short enough and the helicity injection large enough ($\overline{\omega_l} \sim 5 \times 10^{-6}$ s^{-1}), the helicity injection can dominate the combined nonlocal effects of differential rotation and surface diffusion.

From the results discussed above, we conclude that the previous methods applied for helicity injection and the new effect of supergranular helicity injection are complementary in the rising phase of the solar cycle. In the declining phase of the cycle, however, supergranular helicity injection adds new features not found in the previous simulations. In the combined model, exceptions to the hemispheric pattern may still occur, depending on the relative values of the vorticity, differential-rotation gradient, and latitudinal separation of field lines overlying the PIL. It should be noted that, even if the vorticity magnitude is not sufficient to completely overcome differential rotation on an east–west PIL, it can reduce the effect of differential rotation enough to produce the dominant chirality pattern in each hemisphere. This pattern will form as both differential rotation and supergranular helicity injection produce the same chirality on north–south oriented PILs. This implies the existence of a preferred site for the location of negative/positive helicity in the northern/southern hemispheres, which can in principle be tested observationally.

Another possible observational test of the helicity injection mechanism for the corona lies in the topology of the resulting filament channel. Supergranular helicity injection and condensation tend to produce a primarily sheared field at a PIL, whereas flux diffusion and cancellation invariably produce a strongly twisted filament channel. This difference is most easily seen in Figure 3, which contrasts the magnetic topology resulting from supergranular injection only with that produced by differential rotation/cancellation only. It is evident that the filament channel due to cancellation has a much stronger twist, which has important implications both for observational tests and for the possible mechanisms underlying filament eruptions (e.g., Forbes et al. 2006).

For the simulations described above, the effect of helicity injection due to convective cells has only been considered relative to differential rotation and not to the injection of magnetic helicity within new magnetic bipoles. This is a consequence of assuming a potential field for the initial condition. The question now arises as to how the internal helicity of the bipole would effect the results. If the bipole emerges with the dominant sign of helicity for each hemisphere, then along the north–south PIL of the bipole, the same sign of helicity is injected by all three methods. The effect of the additional helicity injection from the emerging bipole would be to shorten the time of formation of the axial field along the PIL. Previous simulations (Mackay & van Ballegooijen 2001) have shown that, in the declining phase, helicity injection during emergence does not overcome the effect of differential rotation on the east–west lead arm (see also Yeates & Mackay 2012). Therefore, the inclusion of a bipole with self-helicity would not change the results presented here for the simple magnetic-field configurations considered.

While the results presented in this paper are encouraging, a number of further studies need to be carried out. First, new observations are required to determine the rate of vorticity within convective cells and its corresponding variation with latitude. In addition, it must be determined whether the hemispheric pattern of filaments still holds in the declining phase of the solar cycle. Next, the six-month comparison between the flux transport simulations and 109 filaments carried out by Yeates et al. (2008) should be rerun with the supergranular helicity injection included. It must be shown that including the small-scale helicity injection in the simulation still reproduces the exceptions, in addition to the dominant hemispheric pattern of chirality. Finally, the full solar cycle simulations of Yeates & Mackay (2012) should be rerun to determine the consequence of different rates of supergranular vorticity on the hemispheric pattern throughout solar cycle 23. Within this study, the effect of latitudinal variations of the vorticity also should be investigated.

D.H.M. would like to thank STFC, the Leverhulme Trust, and the European Commission's Seventh Framework Programme (FP7/2007-2013) under grant agreement SWIFF (project 263340, http://www.swiff.eu) for their financial support. C.R.D. and S.K.A. wish to acknowledge the NASA TR&T and SR&T programs for supporting their contributions to the work. All of us thank Judy Karpen for lending her artistic expertise in creating the figures used in the Appendix and for helpful comments on the manuscript. We also appreciate Anthony Yeates' alerting us to the observations of J. A. Bonet and collaborators. D.H.M. and C.R.D. participated in a team investigation of solar prominences at the International Space Science Institute, where this collaboration was conceived and initiated. We are grateful to ISSI for hosting us, to Nicolas Labrosse for leading the team, and to Zoran Mikić and the rest of the group for stimulating discussions.

APPENDIX

Here, we derive the large-scale helicity injection rate associated with an ensemble of small-scale cyclonic convection cells. For simplicity, consider a vertical magnetic field rooted in a horizontal plane, the photosphere, as shown schematically in Figure 13. We begin with an isolated flux tube being twisted by an individual cell lying in the plane, S. Suppose that the cyclone's average rotation rate is ω_l and scale length (radius) is l, and that its average signed magnetic field in the vertical direction

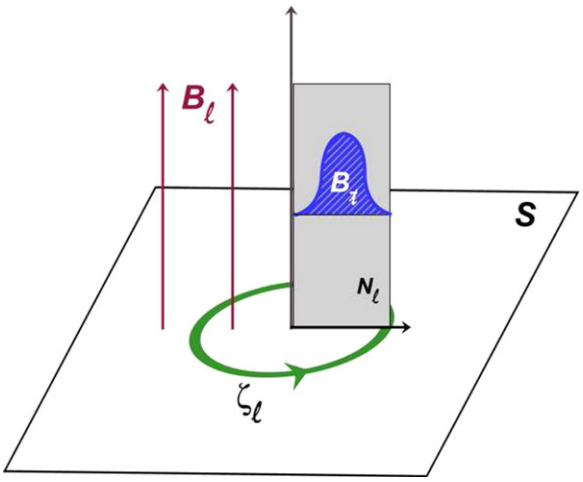

Figure 13. Schematic diagram of the twist flux density B_t (blue-shaded line plot in the vertical plane N_l) induced by cyclonic convection ζ_l (green circle in the horizontal plane S) acting on the radial field B_l (red arrows) in a single convection cell.

(A color version of this figure is available in the online journal.)

is B_l, so that its total signed vertical flux is $\Phi_l = \pi l^2 B_l$. Over a time interval δt, the cyclonic motions induce an azimuthal flux change $\delta\Psi_l$,

$$\begin{aligned}\frac{\delta\Psi_l}{\delta t} &= -\omega_l \Phi_l/2\pi \\ &= -l^2\omega_l B_l/2 \\ &\equiv -\zeta_l B_l,\end{aligned}$$

passing through a vertical plane section N_l that extends from the cyclone's center to its edge and upward from the plane of motion, S. We have introduced the cyclonic parameter $\zeta_l \equiv l^2\omega_l/2$, which measures the strength of the vortical motions in twisting the vertical field and has the dimensions of a diffusivity. The signed flux density, i.e., the twist component of the magnetic field, is denoted B_t and plotted in the figure. The flux change $\delta\Psi_l$ can be represented by a change δA_l in the component of the vector potential that lies in S and is directed away from the center of the cyclonic cell,

$$\begin{aligned}\frac{\delta A_l}{\delta t} l &= -\frac{\delta\Psi_l}{\delta t} \\ &= +\zeta_l B_l,\end{aligned}$$

since the azimuthal flux passing through N_l equals the line integral of the vector potential around its perimeter. The magnetic helicity injected, δH_l, due to the linking of the fluxes by the cyclonic motion is given by

$$\begin{aligned}\frac{\delta H_l}{\delta t} &= \Phi_l \frac{\delta\Psi_l}{\delta t} \\ &= -\omega_l \Phi_l^2/2\pi \\ &= -\zeta_l B_l \Phi_l.\end{aligned}$$

The sign convention employed is that a positive rotation rate corresponds to a right-handed or anti-clockwise motion, which for positive B_l induces a negative azimuthal flux with left-handed twist, i.e., having a negative magnetic helicity. If the sign (handedness) of the rotation is reversed, then so is that of

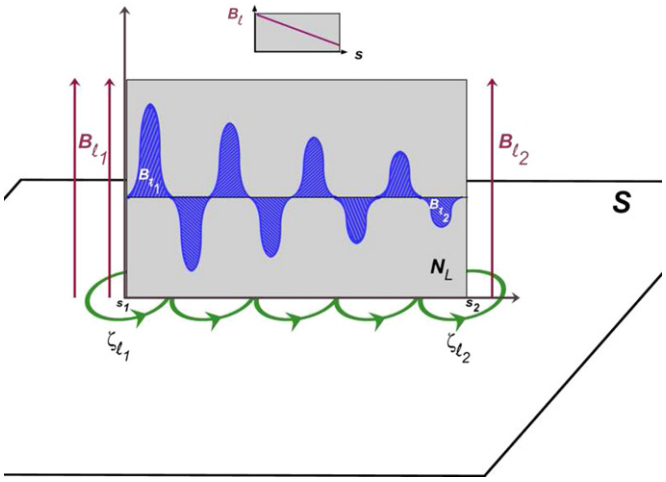

Figure 14. Schematic diagram of the twist flux density B_t (blue-shaded line plot in the vertical plane N_L) induced by cyclonic convection cells ζ_l (green circles in the horizontal plane S) acting on the varying radial field B_l (red arrows). The direction (sign) of the twist flux, toward (positive) and away from (negative) the viewer, alternates across each full cyclonic cell, leaving net contributions from the endpoints s_1 and s_2 of N_L. These end-point contributions differ from one another if the vertical field B_l varies in strength across the region, as shown in the inset graph (red line plot at top). The contributions will also differ if the twisting ζ_l by the cyclonic motions varies in strength across the region.

(A color version of this figure is available in the online journal.)

the helicity (twist). On the other hand, if the sign of the vertical field B_l is reversed, but the handedness of the twist is unchanged, then the sign of the helicity is also unchanged.

Now, we accumulate the contributions to the twist flux and magnetic helicity of multiple cyclonic cells over larger scales. Consider a longer vertical plane section N_L that extends beyond the boundary of the first cyclone to the center of a remote second cyclone, as shown in Figure 14. The footprint of N_L on S will include arbitrary chords cutting through other cyclonic cells along the way; however, the net azimuthal flux through N_L contributed by all such intervening cells is zero. As time passes, reconnection between the oppositely signed twist fluxes on adjacent cyclonic cells will smooth out these small-scale local variations, leaving only the background variation due to large-scale gradients in the rate of twist-flux generation. Therefore, the net flux change $\delta\Psi_L$ and vector-potential change δA_L along the footprint of N_L are simply the algebraic sums of the contributions by the two cyclonic cells at the end points. Positioning those points at linear coordinates s_1 and $s_2 = s_1 + L$, we have

$$\frac{\delta\Psi_L}{\delta t} = -\zeta_l B_l|_{s_1} + \zeta_l B_l|_{s_2}.$$

The corresponding expression for δA_L then takes the form

$$\frac{\delta A_L}{\delta t} = -\frac{\zeta_l B_l|_{s_2} - \zeta_l B_l|_{s_1}}{s_2 - s_1}.$$

We wish to apply this equation on scales δt and L that are large compared to the time and spatial scales of individual cyclones but still small compared to those of a filament channel or PIL. That is, we are interested only in the global long-term evolution of the corona, not in its structure and dynamics on the supergranular (i.e., cyclonic) scales. Over those large scales, the effect of the reconnection-driven helicity condensation is to smooth out the small-scale temporal and spatial fluctuations associated with the individual cyclonic motions (Antiochos 2013). The variations on the left- and right-hand sides above then can be approximated as derivatives; also converting both sides to vector form, we obtain

$$\frac{\partial \mathbf{A}_s}{\partial t} = -\nabla_s (\zeta B_r). \tag{A1}$$

Here, $\mathbf{A}_s$ is the vector potential and ∇_s is the gradient operator including only surface terms (along θ and ϕ on the sphere), and B_r and ζ are the large-scale, averaged values of B_l and ζ_l, respectively.

The helicity source in Equation (A1) induces a horizontal twist component $\mathbf{B}_s$ in the low-coronal magnetic field wherever ζB_r is nonuniform over the surface. It leaves the radial component, B_r, unchanged, since from the induction equation (3) we have

$$\frac{\partial B_r}{\partial t} = -\hat{\mathbf{r}} \cdot \nabla_s \times \nabla_s(\zeta B_r) \equiv 0.$$

On the other hand, the horizontal component adjacent to the surface, $\mathbf{B}_s$, evolves according to

$$\frac{\partial \mathbf{B}_s}{\partial t} = -\nabla_r \times \nabla_s(\zeta B_r),$$

where ∇_r is the radial component of the gradient operator. It is numerically convenient to interchange the order of differentiation in this expression, so that

$$\frac{\partial \mathbf{B}_s}{\partial t} = +\nabla_s \times \nabla_r(\zeta B_r).$$

This is consistent with a time-varying vector potential $A_r\hat{\mathbf{r}}$ that obeys

$$\frac{\partial A_r}{\partial t}\hat{\mathbf{r}} = +\nabla_r (\zeta B_r), \tag{A2}$$

which also leaves B_r unchanged. This alternative form of the helicity-injection term was implemented and used in the global-evolution calculations of this paper (cf. Equations (3) and (4)).

When the vector potential evolves due to the derived helicity injection term, Equation (A1) or (A2), the current-free field $\mathbf{B}_p$ and its vector potential $\mathbf{A}_p$ do not change (because B_r does not change, as shown above). The relative helicity in Equation (7) then evolves according to

$$\frac{dH_r}{dt} = \int_V \left[\frac{\partial \mathbf{A}_s}{\partial t} \cdot (\mathbf{B} - \mathbf{B}_p) + (\mathbf{A} + \mathbf{A}_p) \cdot \frac{\partial \mathbf{B}_s}{\partial t} \right] d\tau.$$

After substituting for the time derivatives from the expressions given in the previous paragraph and for $\mathbf{B} - \mathbf{B}_p = \nabla \times (\mathbf{A} - \mathbf{A}_p)$, then performing integrations by parts and using well-behaved boundary conditions on $\mathbf{A}$, the rate of change of helicity ultimately reduces to the integral

$$\frac{dH_r}{dt} = -2 \int_{R_\odot} \zeta B_r^2 d\sigma \tag{A3}$$

evaluated over the entire surface of the Sun. Restricting the integration to a single cyclonic cell of radius l, where $B_r = B_l$

and $\zeta = \zeta_l = l^2\omega_l/2$, we obtain

$$\begin{aligned}\frac{dH_r}{dt} &= -2\pi \int \omega_l B_l^2 l^3 dl \\ &= -\pi l^4 \omega_l B_l^2/2 \\ &= -\omega_l \Phi_l^2/2\pi \\ &= \frac{\delta H_l}{\delta t},\end{aligned}$$

the result derived at the outset of the Appendix. Thus, we find that our proposed large-scale helicity injection term yields a total helicity injection rate equal to the surface integral of the local rates associated with individual cyclonic cells. This equality must hold when helicity is conserved as reconnection and condensation transport the twist flux to the largest available scales. Our derived expression satisfies this critical requirement.

We emphasize that the helicity-injection model expressed here by Equation (A1) (or A2) is only a statistical approximation that describes the large-scale evolution. It does not replicate any of the complex convection and reconnection dynamics that occur on short spatial and temporal scales, whether those of the cyclonic motions in the low solar atmosphere or of the transient reconnecting current sheets formed between twisted flux tubes in the overlying corona. A first-principles model that attempted to capture all of this physics in 3D over the whole Sun would be prohibitively expensive to run and to analyze. Our prescription instead seeks to capture the evolution averaged over time and space scales that are large compared to those characterizing the convection and reconnection processes but still small compared to the formation and life times and the spatial extent of filament channels. This approach is entirely analogous in spirit to that underlying the continuum diffusion model of the large-scale solar magnetic field, which approximates the cumulative effects of discrete random walks of elementary flux tubes in the photospheric convection (Leighton 1964).

As a consequence of this implicit averaging over small scales, our model yields negligible twist field in any region where the product ζB_r is approximately uniform across the surface. Of course, in such regions where the radial field is uniform and nonzero and the cyclonic motions are acting, nonzero twist fields will be produced locally and be present all the time. As described in Antiochos (2013), however, this twist reaches a low saturation level and does not grow due to its transport by reconnection to larger scales. We expect a long-term growth of the twist field only near PILs where there is a large-scale, persistent variation in the average radial field strength. This is expressed by the twist-field generation term $\nabla_s(\zeta B_r)$. In the simulations in this paper, we assume that ζ is uniform, so that the resulting twist fields tend to accumulate primarily at PILs, where $\nabla_s B_r$ is large. In principle, the twist fields could also grow in regions where the radial-field gradients are strong, even if far from the PIL. However, the same cyclonic convective motions that produce the twist field from the vertical field also shuffle the magnetic flux elements across the surface. The resulting large-scale diffusion will smooth out any radial-field gradients over time, while transporting the twist flux to the PILs. Our simulations, therefore, capture to a good approximation, the smoothing of radial-field gradients and the concentration of twist at PILs, as observed on the Sun.

REFERENCES

Antiochos, S. K. 2013, ApJ, 772, 72
Aulanier, G., & Démoulin, P. 1998, A&A, 329, 1125
Berger, M. A. 1984, GApFD, 30, 79
Bonet, J. A., Màrquez, I., Sànchez Almeida, J., Cabello, I., & Domingo, V. 2008, ApJL, 687, L131
Bonet, J. A., Márquez, I., Sánchez Almeida, J., et al. 2010, ApJL, 723, L139
DeVore, C. R. 2000, ApJ, 539, 944
DeVore, C. R., Sheeley, N. R., Jr, Boris, J. P., Young, T. R., Jr., & Harvey, K. L. 1985, SoPh, 102, 41
Duvall, T. L., Jr. 1979, SoPh, 63, 3
Duvall, T. L., Jr, & Gizon, L. 2000, SoPh, 192, 177
Finn, J. M., & Antonsen, T. M. 1985, CoPPC, 9, 111
Forbes, T. G., Linker, J. A., Chen, J., et al. 2006, SSRv, 123, 251
Foukal, P. 1971a, SoPh, 19, 59
Foukal, P. 1971b, SoPh, 20, 298
Gaizauskas, V. 1998, in ASP Conf. Ser. 150, New Perspectives on Solar Prominences, ed. D. F. Webb, B. Schmieder, & D. M. Rust (IAU Colloq. 167; San Francisco, CA: ASP), 257
Gaizauskas, V. 2002, SoPh, 211, 179
Gizon, L., & Duvall, T. L., Jr. 2003, in ESA Special Publication, Vol. 517, GONG 2002, Local and Global Helioseismology: The Present and Future, ed. H. Sawaya-Lacoste (Noordwijk: ESA), 43
Komm, R., Howe, R., Hill, F., et al. 2007, ApJ, 667, 571
Leighton, R. B. 1964, ApJ, 140, 1547
Leroy, J.-L., Bommier, V., & Sahal-Brechot, S. 1983, SoPh, 83, 135
Leroy, J.-L., Bommier, V., & Sahal-Brechot, S. 1984, A&A, 131, 33
Mackay, D. H., Gaizauskas, V., & van Ballegooijen, A. A. 2000, ApJ, 544, 1122
Mackay, D. H., Karpen, J. T., Ballester, J. L., Schmieder, B., & Aulanier, G. 2010, SSRv, 151, 333
Mackay, D. H., Longbottom, A. W., & Priest, E. R. 1999, SoPh, 185, 87
Mackay, D. H., & van Ballegooijen, A. A. 2001, ApJ, 560, 445
Mackay, D. H., & van Ballegooijen, A. A. 2005, ApJL, 621, L77
Mackay, D. H., & van Ballegooijen, A. A. 2006, ApJ, 641, 577
Mackay, D., & Yeates, A. 2012, LRSP, 9, 6
Martin, S. F. 1998, SoPh, 182, 107
Martin, S. F., Bilimoria, R., & Tracadas, P. W. 1994, in Solar Surface Magnetism, ed. R. J. Rutten & C. J. Schrijver (Dordrecht: Kluwer), 303
Martres, M. J., Michard, R., & Soru-Iscovici, I. 1966, AnAp, 29, 249
Minarovjech, M., Rybansky, M., & Rusin, V. 1998, SoPh, 177, 357
Mouradian, Z., & Soru-Escaut, I. 1994, A&A, 290, 279
Pevtsov, A. A., Balasubramaniam, K. S., & Rogers, J. W. 2003, ApJ, 595, 500
Pevtsov, A. A., Canfield, R. C., & Metcalf, T. R. 1995, ApJL, 440, L109
Rust, D. M. 1967, ApJ, 150, 313
Sheeley, N. R., Jr. 2005, LRSP, 2, 5
Snodgrass, H. B. 1983, ApJ, 270, 288
Taylor, J. B. 1974, PhRvL, 58, 1139
Taylor, J. B. 1986, RvMP, 58, 741
van Ballegooijen, A. A. 2004, ApJ, 612, 519
van Ballegooijen, A. A., Cartledge, N. P., & Priest, E. R. 1998, ApJ, 501, 866
van Ballegooijen, A. A., Priest, E. R., & Mackay, D. H. 2000, ApJ, 539, 983
Yang, W. H., Sturrock, P. A., & Antiochos, S. K. 1986, ApJ, 309, 383
Yeates, A. R., & Mackay, D. H. 2009a, SoPh, 254, 77
Yeates, A. R., & Mackay, D. H. 2009b, ApJ, 699, 1024
Yeates, A. R., & Mackay, D. H. 2012, ApJL, 753, L34
Yeates, A. R., Mackay, D. H., & van Ballegooijen, A. A. 2007, SoPh, 245, 87
Yeates, A. R., Mackay, D. H., & van Ballegooijen, A. A. 2008, SoPh, 247, 103
Zhang, J., & Liu, Y. 2011, ApJL, 741, L7
Zhao, L., DeVore, C. R., & Antiochos, S. K. 2013, ApJ, in press